

Beyond Heatmaps: Unsupervised Concept-Graph Reasoning for Interpretable Visual Explanation

Md Mohasin Hossain^{1,2†}, Anar Amirli^{4†*}, Robert Leist¹, Md Abdul Kadir^{1,3} and Daniel Sonntag^{1,3}

¹German Research Center for Artificial Intelligence (DFKI), Saarbrücken, Germany

²Saarland University, Saarbrücken, Germany

³Oldenburg University, Oldenburg, Germany

⁴BEGO GmbH & Co. KG, Bremen, Germany

Abstract

Concept Bottleneck Models (CBMs) provide an intrinsically interpretable alternative to post-hoc explanations. However, existing CBMs often rely on predefined concept vocabularies or supervised annotations, lack explicit concept grounding, and summarize each concept with a single image-level score—discarding spatial recurrence and inter-concept dependencies. We propose a Graph-based Concept Bottleneck Model (G-CBM), an intrinsically interpretable framework that performs unsupervised concept discovery via Non-negative Matrix Factorization (NMF) and represents the discovered concepts as nodes in a per-image concept-graph representation. G-CBM matches region-level features to these concept nodes—providing concept grounding and capturing concept recurrence across the image—and applies a *tunable concept filtering threshold* τ to suppress weak region-level features. A Graph Attention Network (GAT) then performs concept-level reasoning by modeling nonlinear dependencies across nodes. Across ImageNet, HAM10000, PH2, and Derm7pt, G-CBM achieves an average relative AUC improvement of 3.7% over a ResNet-50 baseline. Concept filtering frequently improves predictive performance while inducing selective concept use, achieving peak AUC of 0.96 on PH2 with only 2 of 10 concepts and 0.92 on HAM10000 with 3.8 of 9 concepts. On dermoscopy benchmarks, G-CBM is competitive with supervised approaches requiring external annotations. Deletion/insertion analyses with random ablation controls show that the learned concept ranking faithfully reflects model predictions.

1 Introduction

Deep learning models have achieved remarkable success across computer vision tasks [He *et al.*, 2016; Dosovitskiy *et al.*, 2020], yet their opaque decision processes limit deployment in safety-critical domains [Esteva *et al.*, 2019]. A common remedy is to explain predictions using post-hoc

*Work performed while affiliated with Saarland University.

†Equal contribution.

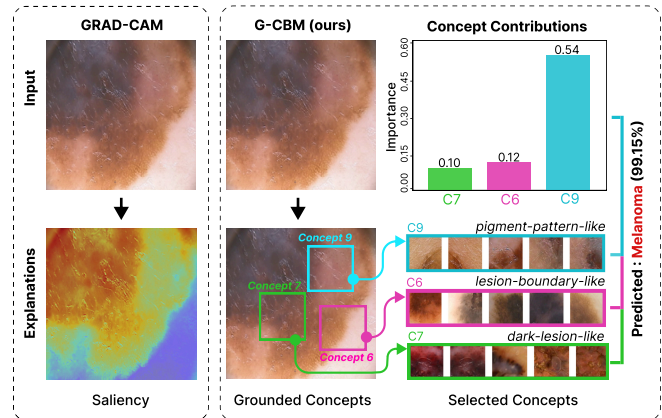


Figure 1: G-CBM produces an interpretable melanoma diagnosis (99.15%) on a dermoscopy image. *Left*: Grad-CAM yields a diffuse pixel-level saliency map. *Right*: G-CBM jointly provides *concept selection* (what concepts drive the prediction: *pigment-pattern-like*, *lesion-boundary-like*, *dark-lesion-like*), *concept grounding* (where they appear, shown as bounding boxes), and *importance scores* (how much each contributes, shown as a bar chart).

saliency-based methods such as Grad-CAM [Selvaraju *et al.*, 2017] or Integrated Gradients [Sundararajan *et al.*, 2017]. Although these methods can highlight discriminative image regions, they operate at the pixel level and provide limited insight into the visual concepts influencing a prediction, and several fail basic sanity checks [Adebayo *et al.*, 2018]. As illustrated in Fig. 1 (left), Grad-CAM produces only a diffuse, unstructured saliency map that highlights image regions without identifying *what* they represent. Post-hoc concept-based methods offer a more structured alternative to these saliency methods by explaining predictions through intermediate concepts rather than raw pixels [Fel *et al.*, 2023b; Patrício *et al.*, 2023]. However, these methods do not perform concept-level reasoning within the prediction process.

Concept Bottleneck Models (CBMs) [Koh *et al.*, 2020] integrate interpretability through concept-level reasoning within the prediction process, but still suffer from several limitations. Existing CBMs typically rely on predefined concept vocabularies or supervised concept annotations [Oikarinen *et al.*, 2023; Yuksekogonul *et al.*, 2022], which are expensive to obtain or outsource interpretability to opaque foundation models such as LLMs and CLIP. While the linear classifier

weights provide coarse per-concept attributions (*how much*), they cannot model nonlinear inter-concept dependencies and reduce each concept to a single image-level score, thereby ignoring its recurrence across image regions. Moreover, CBMs lack explicit concept grounding in the input space (*where*), making it difficult to verify whether the predicted concepts correspond to meaningful visual evidence.

Taken together, post-hoc saliency methods answer only *where*; post-hoc concept methods answer *what* concepts are present but do not integrate concepts into the prediction process; and CBMs integrate interpretability into the prediction process and answer *what* and *how much*, but rely on costly supervision or predefined vocabularies, provide weak concept grounding (no *where*), and combine concepts through a linear classifier—ignoring nonlinear inter-concept dependencies.

We propose **Graph-based Concept Bottleneck Models (G-CBM)**, an intrinsically interpretable image classification framework that integrates concept-level reasoning directly into the prediction pipeline. G-CBM extracts region-level features by passing image patches through a frozen backbone. G-CBM discovers visual concepts from these intermediate features using Non-negative Matrix Factorization (NMF) [Fel *et al.*, 2023b], yielding reusable concept bases that capture recurring visual patterns. It constructs a per-image concept-graph representation: a graph with one *concept node* per discovered concept basis, where a concept node aggregates the region-level features of image patches that match its corresponding basis, and a Graph Attention Network (GAT) models nonlinear inter-concept dependencies across all concept nodes. By matching region-level features against concept nodes, G-CBM preserves repeated and spatially distributed concept evidence across the image. This produces three interpretable signals (Fig. 1, right): activated concept nodes perform *concept selection* by indicating *what* concepts influence the prediction, the image regions provide *concept grounding* showing *where* the evidence appears, and gradient-based sensitivities with respect to concept nodes serve as *importance scores* quantifying *how much* each concept contributes.

In summary, our contributions are as follows. First, we propose G-CBM, an intrinsically interpretable framework that jointly performs classification and explanation (Fig. 2). G-CBM combines *unsupervised concept discovery* with graph-based relational reasoning to produce *concept selection*, *concept grounding*, and *importance scores* in a unified pipeline. Second, we introduce a per-image concept-graph representation in which nodes aggregate region-level features and edges, learned via graph attention, capture inter-concept dependencies (Sec. 3.2). Third, we introduce a *tunable concept filtering threshold* τ that suppresses weak region-level features prior to node aggregation, enabling explicit control over explanation selectivity while improving concept grounding (Sec. 3.2, Table 5); on PH2, this yields an AUC of 0.96 using only 2 of 10 available concepts. Finally, we validate G-CBM across four datasets (ImageNet, HAM10000, PH2, Derm7pt), demonstrating an average relative AUC improvement of 3.7% over ResNet-50, competitive performance against supervised dermatology CBMs without requiring manual concept annotations, and faithful concept rankings under deletion/insertion analyses with random ablation controls (Tables 3, 4, 6).

2 Related Work

Our review covers four areas: post-hoc saliency-based methods, post-hoc concept-based methods, graph-based explanation methods, and Concept Bottleneck Models (CBMs).

Post-hoc saliency-based methods produce pixel-level maps highlighting discriminative regions. Grad-CAM [Selvaraju *et al.*, 2017], Integrated Gradients [Sundararajan *et al.*, 2017], and SmoothGrad [Smilkov *et al.*, 2017] indicate *where* a model attends but not the underlying visual concepts. Adedbayo *et al.* [2018] and Kindermans *et al.* [2019] argue that many saliency methods lack reliability and fail sanity checks, motivating research into more structured and semantically meaningful explanations.

Post-hoc concept-based methods move beyond pixels by identifying visual concepts (*what*) in intermediate-layer activations. TCAV [Kim *et al.*, 2018] measures sensitivity to user-defined concept directions. ACE [Ghorbani *et al.*, 2019] discovers concepts by clustering superpixel activations, while CRAFT [Fel *et al.*, 2023b] extracts features from image regions and applies Non-negative Matrix Factorization (NMF), yielding more interpretable, part-based bases than PCA and K-Means—motivating our use of NMF in G-CBM. Concept Relevance Propagation (CRP) [Achtibat *et al.*, 2023] goes furthest among these, conditioning the relevance backward pass on concept-encoding channels to localize concepts in the input while quantifying their contribution. Yet all these methods remain post-hoc: they do not integrate concept discovery or inter-concept dependencies into the prediction pipeline, and none model nonlinear inter-concept dependencies.

Concept Bottleneck Models (CBMs) [Koh *et al.*, 2020] integrate interpretability directly into the prediction pipeline by first identifying concepts and then using them for final classification. This explains *what* concepts contribute to a prediction, with linear classifier weights serving as coarse per-concept attributions (*how much*). However, CBMs typically rely on predefined concept vocabularies or supervised concept annotations. Several extensions address these limitations. Label-Free CBMs [Oikarinen *et al.*, 2023] reduce manual annotation by using Large Language Models (LLMs) to generate candidate concepts and CLIP similarity to score their presence. Causally Structured CBMs [De Felice *et al.*, 2025] incorporate predefined causal relationships among concepts to improve reasoning consistency.

Dermoscopy-specific variants, PCBM [Yuksekgonul *et al.*, 2022], CBE [Patrício *et al.*, 2023], and MICA [Bie *et al.*, 2024] combine concept bottlenecks with vision-language representations for clinically interpretable diagnosis. However, these methods inherit two common drawbacks: they rely on predefined or expert-guided concept vocabularies (or on opaque LLMs and CLIP encoders to generate and match them), thereby outsourcing interpretability to non-interpretability foundation models. They typically retain only global (image-level) scalar concept representations, thereby discarding spatial recurrence; do not explicitly model nonlinear dependencies between concepts and ground *where* each concept appears in the image.

Graph-based methods offer a complementary way to model relational structure. GNNExplainer [Ying *et al.*, 2019] and PGExplainer [Luo *et al.*, 2020] identify nodes, edges, or

subgraphs for explaining predictions, but assume graph-structured inputs and act as post-hoc explainers for trained GNNs. Scene-graph models [Johnson *et al.*, 2018] perform visual reasoning over object relationships but build graphs from detected objects rather than discovered visual concepts. Consequently, existing graph-based approaches do not yield an intrinsically interpretable concept bottleneck framework.

G-CBM addresses these limitations by integrating *unsupervised concept discovery* and graph-based relational reasoning. G-CBM identifies *what* concepts are present by discovering reusable visual concepts from intermediate-layer region features using NMF, then constructs a per-image concept-graph representation in which each node aggregates region-level features matching a discovered concept, preserving spatial recurrence, and a GAT models inter-concept dependencies. Matching region-level features against concept nodes identifies *where* the concepts appear in the input through concept grounding, and gradient-based class-probability sensitivities of concept nodes quantify *how much* each concept contributes. To our knowledge, G-CBM is the first intrinsically interpretable framework combining unsupervised visual concept discovery with graph-attention-based modeling of inter-concept dependencies.

3 Methodology

Our G-CBM framework performs intrinsically interpretable image classification through concept-level reasoning over a concept-graph representation. As shown in Fig. 2, G-CBM first discovers reusable concept bases from region-level features extracted from image patches via Non-negative Matrix Factorization (NMF), and then classifies each image using a Graph Attention Network (GAT).

3.1 Stage I: Unsupervised Concept Basis Discovery

We extract patches of size $h \times w$ with stride ratio ρ from the training images \mathcal{X} , forming a candidate pool $\mathbf{X} \in \mathbb{R}^{N \times c \times h \times w}$ with N patches in total. Each patch is passed independently through a frozen intermediate layer $g(\cdot)$ of a pre-trained backbone, yielding region-level features stacked into an activation matrix

$$\mathbf{A} = g(\mathbf{X}) \in \mathbb{R}^{N \times p_{\text{feat}}}, \quad (1)$$

where p_{feat} is the hidden feature dimension and each row $\mathbf{A}_i^\top \in \mathbb{R}^{p_{\text{feat}}}$ is the region-level feature of the i -th patch.

Following CRAFT [Fel *et al.*, 2023b], we use NMF [Lee and Seung, 1999] for unsupervised concept discovery from \mathbf{A} . NMF finds non-negative vector bases in activation space, where each direction corresponds to a distinct piece of information (e.g., wheel, stripe, glass), and the non-negative coefficient of a sample along a direction tells how strongly that concept is present.

$$\mathbf{S}^*, \mathbf{C}^* \in \arg \min_{\mathbf{S} \geq 0, \mathbf{C} \geq 0} \frac{1}{2} \|\mathbf{A} - \mathbf{S}\mathbf{C}^\top\|_F^2. \quad (2)$$

Here, $\mathbf{C} \in \mathbb{R}^{p_{\text{feat}} \times r}$ holds the r concept bases as columns, while $\mathbf{S} \in \mathbb{R}^{N \times r}$ contains the region-level concept scores used only within Stage I for concept-number selection.

$$\mathbf{A}_i \approx \sum_{v=1}^r s_{iv} \mathbf{c}_v, \quad (3)$$

where $\mathbf{c}_v \in \mathbb{R}^{p_{\text{feat}}}$ is the v -th column of \mathbf{C} . The selected concept bases \mathbf{C} are then frozen and reused as the concept nodes (each concept basis \mathbf{c}_v defines a concept node $v \in \mathcal{V}$ in our per-image concept-graph representation (Sec. 3.2).

Selecting r . For each $k \in \{6, \dots, 16\}$ we score NMF as $\text{Score}(k) = \frac{1}{k} \sum_i D_i - \lambda P_k$, where D_i is concept i 's top-10% patch fraction in its dominant class and P_k penalises class-imbalanced coverage among discriminative concepts ($D_i \geq 0.6$). We set $\lambda = 1$ and pick $r = \arg \max_k \text{Score}(k)$ per (backbone, dataset); selected values in Table 2.

3.2 Stage II: Concept Graph-Based Prediction and Explanation

Projection onto concept basis. For any image x , its n patches $\hat{\mathbf{X}}$ are passed through the backbone $g(\cdot)$, where n denotes the per-image patch count (distinct from N , the total training patch pool used in Sec. 3.1). The resulting region-level features are then projected onto the frozen concept bases \mathbf{C} via Non-negative Least Squares (NNLS):

$$\mathbf{s}_j^* \in \arg \min_{\mathbf{s} \geq 0} \frac{1}{2} \|g(\hat{X}_j) - \mathbf{C}\mathbf{s}\|_2^2, \quad (4)$$

where $\hat{X}_j \in \mathbb{R}^{c \times h \times w}$ is the j -th patch, $g(\hat{X}_j) \in \mathbb{R}^{p_{\text{feat}}}$ is its region-level feature, and $\mathbf{s}_j = [s_{j1}, \dots, s_{jr}]^\top \in \mathbb{R}^r$ contains its region-level concept scores. We build a fully connected concept graph $\mathcal{G} = (\mathcal{V}, \mathcal{E}, \mathbf{H})$ with node set \mathcal{V} of r concept nodes, edge set \mathcal{E} , and node features $\mathbf{H} \in \mathbb{R}^{r \times p_{\text{feat}}}$, preserving repeated and spatially distributed concept evidence across the image.

Concept filtering threshold. Many patches bear only marginal resemblance to any concept, contributing noise to the concept node representations. We therefore introduce a concept filtering threshold $\tau \geq 0$:

$$\tilde{s}_{jv} = s_{jv} \mathbf{1}[s_{jv} \geq \tau]. \quad (5)$$

$\tau \geq 0$ filters patches with marginal concept evidence, controlling explanation selectivity and improving grounding without removing nodes from the fixed graph. At $\tau = 0$, G-CBM reduces to the unthresholded model; if all nodes become inactive at high τ , prediction confidence degrades toward chance. We treat τ as a tunable hyperparameter and select τ^* per (backbone, dataset) on the validation split (Sec. 4.1).

Definition 1 (Active Concept Count). For an image x , a concept node v is active after thresholding if at least one patch contributes positive thresholded evidence, i.e., $\sum_{j=1}^n \tilde{s}_{jv} > 0$. The active concept count $K_\tau(x)$ is the number of such nodes:

$$K_\tau(x) = \sum_{v=1}^r \mathbf{1} \left[\sum_{j=1}^n \tilde{s}_{jv} > 0 \right]. \quad (6)$$

$K_\tau(x)$ measures the explanation selectivity for image x : a smaller value means fewer concepts contribute to the prediction. We report \bar{K}_τ , the mean of $K_\tau(x)$ over the test set, as a dataset-level selectivity measure (see Fig. 3).

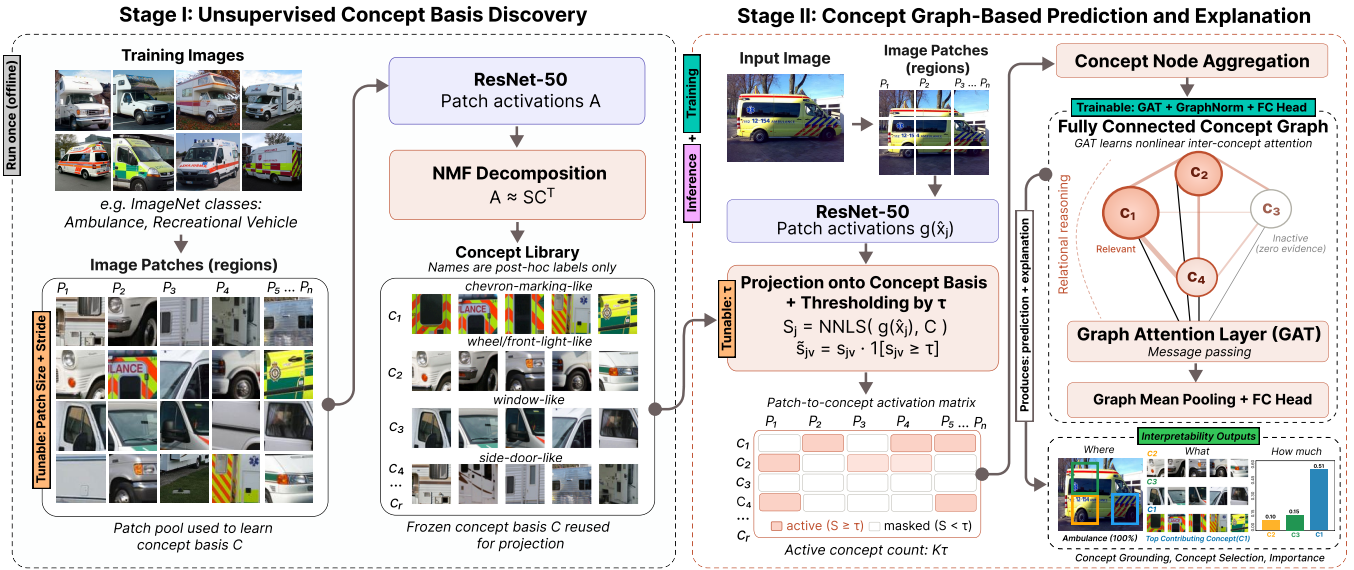


Figure 2: Overview of G-CBM. Stage I: training images are divided into patches (regions) and encoded by a frozen backbone; NMF decomposes the activations to obtain a reusable concept basis C . Stage II: For an input image, region-level features (patch activations) are projected onto C , filtered by the concept filtering threshold τ , and aggregated into concept-specific nodes. A GAT processes the resulting graph for prediction and explanation. Concept names are post-hoc descriptions for visualization only and are not used during training.

Node feature initialization. Each concept node v is initialized by aggregating the region-level features $g(\hat{X}_j)$ weighted by the corresponding thresholded concept scores \tilde{s}_{jv} :

$$\mathbf{h}_v^{(0)} = \text{GELU} \left(\frac{1}{n} \sum_{j=1}^n g(\hat{X}_j) \tilde{s}_{jv} \right), \quad v = 1, \dots, r, \quad (7)$$

where GELU [Hendrycks and Gimpel, 2016] is applied element-wise. The $1/n$ normalization weights each concept by its activation frequency. Stacking $\{\mathbf{h}_v^{(0)}\}_{v=1}^r$ row-wise yields the initial node feature matrix $\mathbf{H} \in \mathbb{R}^{r \times p_{\text{feat}}}$, which is passed to the GAT.

Classification via Graph Attention. The fully connected concept graph is processed with a shallow multi-head GAT [Veličković *et al.*, 2017], allowing each concept node to attend to all others. For head $i \in \{1, \dots, H\}$, with $\mathbf{W}^{(i)} \in \mathbb{R}^{d' \times p_{\text{feat}}}$ and learnable attention vector $\mathbf{a}^{(i)} \in \mathbb{R}^{2d'}$, we compute the attention energy $e_{vu}^{(i)}$ and coefficient $\alpha_{vu}^{(i)}$ from node u to node v as

$$e_{vu}^{(i)} = \text{LeakyReLU} \left(\mathbf{a}^{(i)\top} [\mathbf{W}^{(i)} \mathbf{h}_v^{(0)} \parallel \mathbf{W}^{(i)} \mathbf{h}_u^{(0)}] \right), \quad (8)$$

$$\alpha_{vu}^{(i)} = \frac{\exp(e_{vu}^{(i)})}{\sum_{w \in \mathcal{N}(v)} \exp(e_{vw}^{(i)})}, \quad (9)$$

where $\mathcal{N}(v)$ contains all concept nodes. The attention-head outputs are averaged and then normalized with GraphNorm [Cai *et al.*, 2021] before ELU activation:

$$\bar{\mathbf{m}}_v = \frac{1}{n_h} \sum_{i=1}^{n_h} \sum_{u \in \mathcal{N}(v)} \alpha_{vu}^{(i)} \mathbf{W}^{(i)} \mathbf{h}_u^{(0)}, \quad (10)$$

$$\mathbf{h}_v^{(1)} = \text{ELU}(\text{GraphNorm}(\bar{\mathbf{m}}_v)). \quad (11)$$

The GAT models nonlinear inter-concept dependencies and applies node-specific transformations, so each concept node makes a distinguishable contribution to prediction (Eq. 13); under a linear or MLP head on pooled features, all nodes would contribute identically, collapsing importance scores.

$$\tilde{\mathbf{h}} = \frac{1}{r} \sum_{v=1}^r \mathbf{h}_v^{(1)}, \quad \hat{y} = \text{Softmax}(\mathbf{W}_{\text{cls}} \tilde{\mathbf{h}} + \mathbf{b}_{\text{cls}}). \quad (12)$$

During training, only the GAT and classification head are trained (cross-entropy); the backbone and concept bases remain frozen.

3.3 Interpretability Outputs: Selection, Grounding, and Importance

Concept selection (what). The set of concept nodes with positive thresholded evidence $\{v : \sum_{j=1}^n \tilde{s}_{jv} > 0\}$, of size $K_\tau(x)$ (Def. 1), identifies which concepts influence the prediction for image x .

Importance scores (how much). Let $c^* = \arg \max_c \hat{y}_c$ be the predicted class. The importance of a concept node v for class c^* is measured by the gradient-based sensitivity of the predicted-class probability to the node feature:

$$S_C(v, c^*) = \left\| \frac{\partial \hat{y}_{c^*}}{\partial \mathbf{h}_v^{(0)}} \right\|_1. \quad (13)$$

Ranking concept nodes by S_C quantifies how much each concept contributes to the final decision.

Concept grounding (where). For image x , we identify the most influential concepts by ranking all nodes according to S_C and retaining the top three concepts. To localise each concept in the image, we assign every patch \hat{X}_j a grounding score based on how strongly it activates concepts that contribute to the final prediction:

Backbone	Method	$\ell_2 \downarrow$	Spars. \uparrow	Stab. \downarrow	OOD \downarrow
ResNet-50	PCA	0.38/0.27	0.00/0.00	0.28/0.37	0.15/0.06
	K-Means	0.50/0.37	0.96/0.96	0.01/0.02	0.14/0.05
	NMF	0.40/0.28	0.36/0.35	0.09/0.07	0.16/0.06
DenseNet-201	PCA	0.59/0.41	0.00/0.00	0.33/0.33	0.34/0.13
	K-Means	0.66/0.50	0.96/0.96	0.04/0.04	0.28/0.10
	NMF	0.58/0.40	0.41/0.34	0.14/0.09	0.32/0.11
MobileNet-V2	PCA	0.43/0.30	0.00/0.00	0.36/0.39	0.19/0.07
	K-Means	0.54/0.41	0.96/0.96	0.03/0.03	0.17/0.05
	NMF	0.46/0.32	0.41/0.40	0.12/0.11	0.20/0.07

Table 1: Quality of discovered concepts across backbones and methods (ImageNet/HAM10000 per cell). Metrics follow: ℓ_2 reconstruction error, sparsity, stability, and OOD error. NMF achieves the best overall balance and is used in G-CBM.

$$S_P(j, c^*) = \sum_{v=1}^r \tilde{s}_{jv} S_C(v, c^*). \quad (14)$$

We treat \tilde{s}_{jv} as constants since NNLS is non-differentiable. A patch scores high when it strongly activates concepts important to the decision; for each selected concept, we visualize its top-activating patches (Fig. 4).

4 Experiments and Results

We evaluate G-CBM in terms of classification performance, faithfulness, and spatial interpretability across natural and dermoscopic image datasets.

4.1 Datasets and Setup

Our experiments span four datasets. An **ImageNet** subset [Deng *et al.*, 2009] (2,943 images) evaluates fine-grained differentiation between visually similar categories (Ambulance vs. Recreational Vehicle). The remaining dermoscopy datasets focus on binary melanoma vs. nevus classification: **HAM10000** [Tschandl *et al.*, 2018] ($\sim 7,000$ images), **PH2** [Mendonça *et al.*, 2013] (200 images), and **Derm7pt** [Kawahara *et al.*, 2018] (827 images). All datasets use a 70/15/15 train/val/test split, with minority-class over-sampling applied only to the training split.

Implementation. We use ResNet-50 [He *et al.*, 2016], DenseNet-201 [Huang *et al.*, 2017], and MobileNet-V2 [Sandler *et al.*, 2018] in our experiments. Region-level features come from the last conv layer, patch size 70×70 with a stride ratio $\rho = 0.5$. The GAT uses a hidden dimension of 128 with four attention heads for PH2 and Derm7pt, and six for HAM10000 and ImageNet. Models are trained for up to 300 epochs using AdamW ($\text{lr} = 10^{-3}$, $\text{wd} = 2 \times 10^{-4}$) with early stopping on validation loss. Results are reported as mean \pm std over three runs with seeds $\{42, 123, 456\}$.

Concept Discovery. To verify NMF transfers to dermoscopy, we replicate the PCA/K-Means/NMF comparison across all three backbones on ImageNet and HAM10000 (Table 1). NMF provides a favorable trade-off across reconstruction error, sparsity, stability, and OOD robustness in both domains, confirming its suitability for G-CBM.

Concept Filtering. Since tuning τ^* across datasets and backbones is expensive, we calibrate it on validation: each model is trained once at $\tau = 0$, $\tau \in \{0.1, \dots, 1.0\}$ is applied

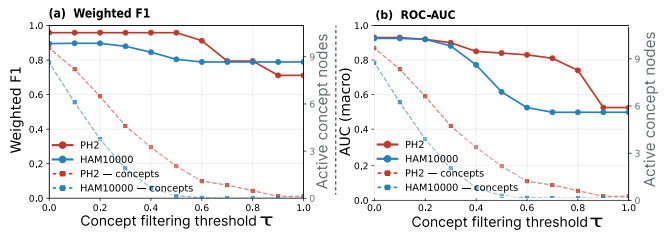


Figure 3: Concept selectivity vs. classification performance on PH2 and HAM10000. *Left*: weighted F1 (solid) and mean active concept count \bar{K}_τ (dashed) vs. τ . *Right*: AUC (solid) and \bar{K}_τ (dashed) vs. τ . F1 remains elevated at high τ due to class imbalance; AUC better reflects threshold-dependent discriminative quality.

at validation, and τ^* is selected by validation F1 score (Table 2). Fig. 3 plots F1, AUC, and \bar{K}_τ versus τ for PH2 and HAM10000: for small τ , F1 and AUC do not drop significantly, indicating that mild filtering removes noise without sacrificing discriminative information. Models are then retrained at τ^* . Calibration statistics differ from test because filtering shifts the GAT’s input distribution (e.g., PH2/ResNet-50: 0.833 vs. 0.960 after retraining). Table 2 reports the selected τ^* and the corresponding validation statistics for all backbones and datasets. After selecting τ^* , we retrain, validate, and test each model with τ^* applied throughout; final test-set results are reported in Section 4.2.

Dataset	ResNet-50			DenseNet-201			MobileNet-V2		
	τ^*	F1/AUC	\bar{K}_{τ^*}/r	τ^*	F1/AUC	\bar{K}_{τ^*}/r	τ^*	F1/AUC	\bar{K}_{τ^*}/r
HAM10000	0.2	0.894/0.917	3.76/9	0.3	0.880/0.892	3.74/16	0.2	0.884/0.907	2.47/6
PH2	0.5	0.958/0.833	2.04/10	0.3	0.933/0.980	6.08/12	0.4	0.922/0.967	2.28/8
Derm7pt	0.1	0.821/0.885	9.07/12	0.1	0.804/0.852	6.25/7	0.1	0.797/0.832	5.31/7
ImageNet	0.1	0.949/0.989	6.31/8	0.1	0.951/0.994	11.30/16	0.2	0.913/0.977	5.10/10

Table 2: Selected thresholds τ^* and corresponding validation statistics per backbone and dataset, used only for τ^* selection (no test-set numbers here). r : total concept nodes; \bar{K}_{τ^*} : mean active nodes at τ^* . Each cell lists $\tau^*/\text{F1}/\text{AUC}/\bar{K}_{\tau^*}/r$. Means over three seeds. Test-set results obtained after retraining at τ^* are reported in Table 3.

4.2 Classification Performance

Table 3 compares G-CBM with CNN baselines across all four datasets and three backbones, and with CBM (linear) and CBM (MLP) on all four datasets using ResNet-50. G-CBM (ResNet-50) improves average AUC over the ResNet-50 baseline by 3.7% relative, and beats the strongest CNN on HAM10000 (0.923 vs. 0.912) and ImageNet (0.984 vs. 0.980); with DenseNet-201, G-CBM achieves the highest ImageNet AUC overall (0.985). On PH2, G-CBM (ResNet-50, $\tau^* = 0.5$) reaches $\text{AUC} = 0.960 \pm 0.006$ with $\bar{K}_{\tau^*} = 2.0$ of $r = 10$ active concept nodes (Table 5), showing that selective high-confidence concept evidence can improve accuracy. Replacing the GAT classifier with linear or MLP classifiers results in suboptimal performance, suggesting that the GAT improves predictive accuracy.

4.3 Comparison with Supervised Methods

Table 4 compares G-CBM with state-of-the-art supervised concept-based approaches on Derm7pt and PH2. Without concept annotations, G-CBM (ResNet-50) achieves 0.868 AUC on Derm7pt, surpassing PCBM, PCBM-h, CBE, and

Model	HAM10000		PH2		Derm7pt		ImageNet	
	AUC	F1	AUC	F1	AUC	F1	AUC	F1
<i>CNN baselines (no concept bottleneck)</i>								
CNN ResNet-50	0.891±.011	0.865±.019	0.903±.096	0.901±.085	0.828±.029	0.791±.014	0.980±.004	0.923±.006
CNN DenseNet-201	0.901±.005	0.877±.008	0.945±.015	0.864±.045	0.850±.030	0.796±.006	0.973±.007	0.922±.012
CNN MobileNet-V2	0.912±.013	0.892±.009	0.943±.005	0.908±.017	0.901±.029	0.848±.012	0.980±.003	0.933±.010
<i>G-CBM (ours, interpretable concept-graph model)</i>								
G-CBM ResNet-50	0.923±.004	0.909±.015	0.960±.006	0.925±.004	0.868±.008	0.823±.019	0.983±.002	0.935±.003
G-CBM DenseNet-201	0.907±.002	0.860±.007	0.937±.015	0.908±.021	0.834±.015	0.786±.009	0.985±.001	0.949±.006
G-CBM MobileNet-V2	0.892±.003	0.865±.009	0.913±.006	0.889±.001	0.830±.005	0.791±.004	0.956±.002	0.908±.006
MLP-CBM (ours) ResNet-50	0.856±.002	0.799±.006	0.897±.006	0.854±.000	0.810±.008	0.762±.005	0.977±.000	0.925±.000
Linear-CBM (ours) ResNet-50	0.850±.000	0.768±.001	0.887±.059	0.866±.020	0.810±.001	0.724±.009	0.971±.002	0.910±.004

Table 3: Test-set classification performance (AUC and F1, mean \pm std, $n = 3$). G-CBM models use the per-dataset optimal τ^* from Table 2. **Bold** = best value per dataset/metric across both baseline and G-CBM groups. MLP-CBM and Linear-CBM replace the GAT with MLP and linear classifiers, respectively.

both MICA variants, and trailing only CAW. On PH2, G-CBM reaches 0.960 AUC and 0.925 F1, outperforming [Sarkar *et al.*, 2022], PCBM, and PCBM-h, while remaining below CBE and MICA variants.

Method	Derm7pt		PH2	
	AUC	F1	AUC	F1
Sarkar <i>et al.</i> [2022]	0.762±.021	0.668±.012	0.793±.006	0.797±.021
PCBM [Yuksekgonul <i>et al.</i> , 2022]	0.730±.014	0.710±.014	0.783±.012	0.815±.026
PCBM-h [Yuksekgonul <i>et al.</i> , 2022]	0.833±.011	0.745±.014	0.923±.015	0.833±.026
CBE [Patrício <i>et al.</i> , 2023]	0.766±.004	0.781±.004	0.976±.000	0.939±.000
MICA (w/ bot) [Bie <i>et al.</i> , 2024]	0.841±.011	0.781±.012	0.977±.012	0.944±.015
MICA (w/o bot) [Bie <i>et al.</i> , 2024]	0.856±.011	0.794±.012	0.982±.014	0.953±.012
CAW [Hou <i>et al.</i> , 2024]	0.886±.001	0.813±.009	—	—
G-CBM (ours) [†]	0.868±.008	0.823±.019	0.960±.006	0.925±.004

Table 4: Comparison with supervised concept-based methods on Derm7pt and PH2 (ResNet-50). Prior-work results (mean \pm std) are reproduced from the original papers; [†] denotes our results at the per-dataset optimal τ^* (Table 2), mean \pm std over $n=3$ seeds. G-CBM is the only method that requires no concept annotations. **Bold** = best per dataset/metric.

4.4 Concept Selectivity

We measure how *selectively* G-CBM uses its concept basis: among the r available nodes, how many actually contribute to each prediction (\bar{K}_τ , Def. 1). Table 5 reports test-set results at the calibrated τ^* (Sec. 4.1). On PH2, F1 *improves* from 0.887 at $\tau = 0$ to 0.925 at $\tau^* = 0.5$ while \bar{K}_{τ^*} drops from 10 to 2.0; on HAM10000, peak F1 of 0.909 is reached at $\tau^* = 0.2$ with only 3.8 of 9 nodes active. F1 alone can be misleading under class imbalance, but AUC at τ^* (0.923–0.983 across datasets) confirms the gain is genuine. G-CBM’s predictions are thus anchored in a *selective, high-confidence subset of concept evidence*—on PH2 and HAM10000, 20–42% of available concepts suffice; on Derm7pt and ImageNet, more concepts remain active, reflecting greater visual heterogeneity rather than diffuse averaging.

4.5 Faithfulness Analysis

We assess whether the GAT’s gradient-ranked concept importance forms a *faithful* explanatory signal via deletion/insertion analysis, a standard perturbation-based evaluation in XAI [Samek *et al.*, 2016; Petsiuk *et al.*, 2018; Fel *et al.*, 2023a; Achibat *et al.*, 2023]. For each test image we compare two rankings of the r concept nodes: *Most-Relevant-First (MRF)*, nodes ranked by $S_C(v, c^*)$ (Eq. 13),

Dataset	r	F1 ($\tau=0$)	τ^*	F1 (τ^*)	AUC (τ^*)	\bar{K}_{τ^*}
HAM10000	9	0.885±.005	0.2	0.909±.015	0.923±.004	3.8
PH2	10	0.887±.002	0.5	0.925±.004	0.960±.006	2.0
Derm7pt	12	0.806±.019	0.1	0.823±.019	0.868±.008	9.0
ImageNet	8	0.944±.006	0.1	0.935±.003	0.983±.002	6.4

Table 5: Test-set concept selectivity (ResNet-50). r : total concept nodes; \bar{K}_{τ^*} : mean active nodes at τ^* . F1 at $\tau = 0$ is the unfiltered baseline; models are retrained with τ^* applied throughout. AUC confirms the gain is not an F1-only artefact on imbalanced datasets.

and *Random*, a uniformly sampled permutation serving as a no-information control. Deletion progressively zeroes the top- $\lfloor fr \rfloor$ node features for $f \in \{0, 0.1, \dots, 1\}$; insertion restores them from an all-zero state. We summarise each 11-point curve by trapezoidal AUC: AUC_{del} (\downarrow) and AUC_{ins} (\uparrow). Across all four datasets (Table 6), MRF outperforms the random baseline with AUC_{del} lower by 10–16 points and AUC_{ins} higher by 5–10 points, confirming that gradient-ranked concept importance carries genuine explanatory signal.

Dataset	$AUC_{\text{del}} \downarrow$		$AUC_{\text{ins}} \uparrow$	
	MRF	Random	MRF	Random
HAM10000	0.767±.171	0.872±.154	0.922±.126	0.871±.158
PH2	0.742±.260	0.899±.147	0.967±.037	0.868±.175
Derm7pt	0.611±.064	0.770±.124	0.861±.132	0.766±.128
ImageNet	0.706±.238	0.855±.154	0.941±.085	0.863±.151

Table 6: Faithfulness of concept-node importance rankings via deletion/insertion analysis. AUC computed by trapezoidal integration over $f \in [0, 1]$ (11 points); \pm = per-image std. MRF = Most-Relevant-First (gradient-ranked). Lower AUC_{del} and higher AUC_{ins} indicate more faithful explanations.

4.6 Spatial Interpretability

Figure 4 shows concept-level explanations for three correctly classified images spanning all three data domains: a PH2 melanoma, a HAM10000 melanocytic nevus, and an ImageNet ambulance. In each case, the model identifies a small set of localized concepts, assigns them class-relevant importance scores, and retrieves exemplar patches that support their interpretation. The examples show that concept evidence remains spatially concentrated and semantically coherent across domains: the melanoma case highlights the lesion core, the nevus case emphasizes the lesion boundary,

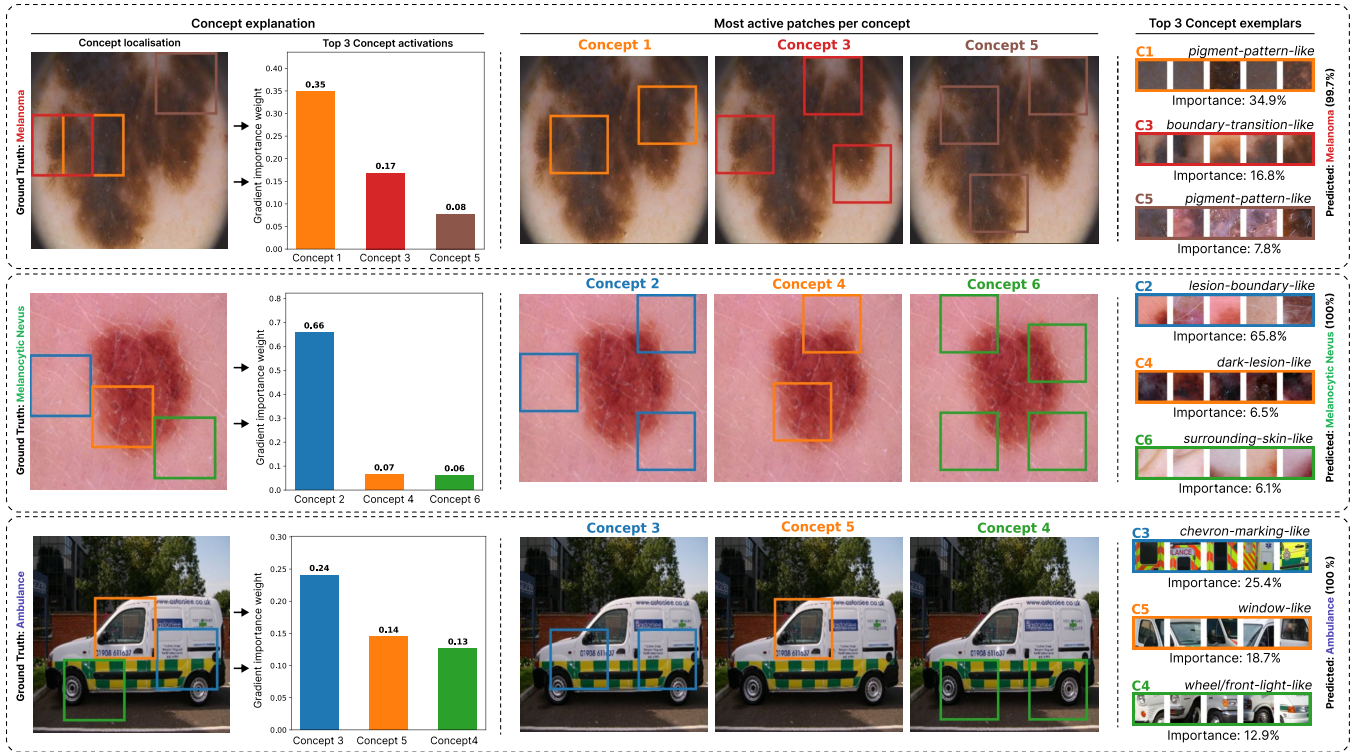


Figure 4: Concept-level spatial explanations on PH2, HAM10000, and ImageNet, illustrating G-CBM’s three interpretability outputs: *concept selection* (top-3 concept nodes), *concept grounding* (coloured bounding boxes), and *importance scores* ($S_C(v, c^*)$, Eq. 13, normalised over the top-3). Each row also shows per-concept activation overlays and exemplar patches retrieved by highest NMF score s_{jv} . Row 1 (PH2 – Melanoma, 99.7%): top concept node (orange, $S_C=0.35$) on the atypical pigment network at the lesion centre. Row 2 (HAM10000 – Nevus, 100%): dominant concept node (blue, $S_C=0.66$) along the lesion boundary and adjacent skin. Row 3 (ImageNet – Ambulance, 100%): top concept node on chevron-style markings; additional nodes cover side window/signage and lower vehicle structure. “-like” descriptors are post-hoc summaries of retrieved exemplars, not training supervision.

and the ambulance case separates vehicle markings from surrounding structural regions. This consistency indicates that G-CBM learns concept-level evidence that is both localizable and transferable beyond dermoscopy.

4.7 Patch-Stride Ablation

We systematically investigate the effect of the patch extraction hyperparameters via a grid search over patch sizes $p \in \{48, 64, 70, 80, 96, 112\}$ and stride ratios $\rho \in \{0.25, 0.35, 0.50, 0.65, 0.80\}$ for G-CBM (ResNet-50) on all four datasets. Table 7 reports selected results with a standard ResNet-50 CNN baseline as reference. The setting $p = 70$, $\rho = 0.5$ outperforms the CNN baseline on all three metrics (AUC, F1, Accuracy) in three of four datasets (HAM10000, Derm7pt, ImageNet; PH2 is the exception at this stage) and was selected as the universal default.

5 Conclusion

We introduced G-CBM, an intrinsically interpretable framework for visual classification that combines unsupervised concept discovery (via NMF) with graph attention over a per-image concept-graph. G-CBM jointly produces *concept selection* (what), *concept grounding* (where), and *importance scores* (how much) within the prediction pipeline, without requiring supervised concept annotations, LLM/CLIP-assisted discovery, or post-hoc analysis on a pretrained model.

Model	p/ρ	HAM	PH2	D7	IN	✓
CNN	—	0.876	0.920	0.819	0.977	
G-CBM	48 / 0.5	0.881	0.890	0.812	0.945	
G-CBM	70 / 0.5	0.928	0.910	0.863	0.985	✓
G-CBM	96 / 0.65	0.920	0.900	0.859	0.970	
G-CBM	112 / 0.5	0.924	0.895	0.851	0.978	✓

Table 7: Patch-stride ablation (AUC on test split). ResNet-50 CNN is the baseline. HAM = HAM10000; D7 = Derm7pt; IN = ImageNet. **Bold** marks the best G-CBM value among the selected patch-stride settings for each dataset. ✓ indicates all three metrics (AUC, F1, Acc) exceed the CNN baseline on at least 3 of 4 datasets.

G-CBM improves average AUC by 3.7% relative over ResNet-50 across four datasets. The concept filtering threshold τ yields selective, high-confidence explanations: on PH2, only two of ten concept nodes are active on average. Deletion/insertion analysis with random-ordering controls confirms that concept importance carries a genuine explanatory signal. G-CBM’s patch representation depends on sufficient resolution and can fragment structures at patch boundaries; overlapping patches partly mitigate this, and segmentation-guided extraction is a natural next step. Overall, G-CBM shows that visual classifiers can reason through localised, reusable concepts without sacrificing predictive performance.

References

- [Achtibat *et al.*, 2023] Reduan Achtibat, Maximilian Dreyer, Ilona Eisenbraun, Sebastian Bosse, Thomas Wiegand, Wojciech Samek, and Sebastian Lapuschkin. From attribution maps to human-understandable explanations through concept relevance propagation. *Nature machine intelligence*, 5(9):1006–1019, 2023.
- [Adebayo *et al.*, 2018] Julius Adebayo, Justin Gilmer, Michael Muell, Ian Goodfellow, Moritz Hardt, and Been Kim. Sanity checks for saliency maps. *Advances in neural information processing systems*, 31, 2018.
- [Bie *et al.*, 2024] Yequan Bie, Luyang Luo, and Hao Chen. Mica: Towards explainable skin lesion diagnosis via multi-level image-concept alignment. In *Proceedings of the AAAI Conference on Artificial Intelligence*, volume 38, pages 837–845, 2024.
- [Cai *et al.*, 2021] Tianle Cai, Shengjie Luo, Keyulu Xu, Di He, Tie-yan Liu, and Liwei Wang. Graphnorm: A principled approach to accelerating graph neural network training. In *International Conference on Machine Learning*, pages 1204–1215. PMLR, 2021.
- [De Felice *et al.*, 2025] Giovanni De Felice, Arianna Casanova Flores, Francesco De Santis, Silvia Santini, Johannes Schneider, Pietro Barbiero, and Alberto Termine. Causally reliable concept bottleneck models. *arXiv preprint arXiv:2503.04363*, 2025.
- [Deng *et al.*, 2009] Jia Deng, Wei Dong, Richard Socher, Li-Jia Li, Kai Li, and Li Fei-Fei. Imagenet: A large-scale hierarchical image database. In *2009 IEEE conference on computer vision and pattern recognition*, pages 248–255. Ieee, 2009.
- [Dosovitskiy *et al.*, 2020] Alexey Dosovitskiy, Lucas Beyer, Alexander Kolesnikov, Dirk Weissenborn, Xiaohua Zhai, Thomas Unterthiner, Mostafa Dehghani, Matthias Minderer, Georg Heigold, Sylvain Gelly, et al. An image is worth 16x16 words: Transformers for image recognition at scale. *arXiv preprint arXiv:2010.11929*, 2020.
- [Esteva *et al.*, 2019] Andre Esteva, Alexandre Robicquet, Bharath Ramsundar, Volodymyr Kuleshov, Mark DePristo, Katherine Chou, Claire Cui, Greg Corrado, Sebastian Thrun, and Jeff Dean. A guide to deep learning in healthcare. *Nature medicine*, 25(1):24–29, 2019.
- [Fel *et al.*, 2023a] Thomas Fel, Victor Boutin, Louis Béthune, Rémi Cadène, Mazda Moayeri, Léo Andéol, Mathieu Chalvidal, and Thomas Serre. A holistic approach to unifying automatic concept extraction and concept importance estimation. *Advances in Neural Information Processing Systems*, 36:54805–54818, 2023.
- [Fel *et al.*, 2023b] Thomas Fel, Agustin Picard, Louis Bethune, Thibaut Boissin, David Vigouroux, Julien Colin, Rémi Cadène, and Thomas Serre. Craft: Concept recursive activation factorization for explainability. In *Proceedings of the IEEE/CVF conference on computer vision and pattern recognition*, pages 2711–2721, 2023.
- [Ghorbani *et al.*, 2019] Amirata Ghorbani, James Wexler, James Y Zou, and Been Kim. Towards automatic concept-based explanations. *Advances in neural information processing systems*, 32, 2019.
- [He *et al.*, 2016] Kaiming He, Xiangyu Zhang, Shaoqing Ren, and Jian Sun. Deep residual learning for image recognition. In *Proceedings of the IEEE conference on computer vision and pattern recognition*, pages 770–778, 2016.
- [Hendrycks and Gimpel, 2016] Dan Hendrycks and Kevin Gimpel. Gaussian error linear units (gelus). *arXiv preprint arXiv:1606.08415*, 2016.
- [Hou *et al.*, 2024] Junlin Hou, Jilan Xu, and Hao Chen. Concept-attention whitening for interpretable skin lesion diagnosis. In *International Conference on Medical Image Computing and Computer-Assisted Intervention*, pages 113–123. Springer, 2024.
- [Huang *et al.*, 2017] Gao Huang, Zhuang Liu, Laurens Van Der Maaten, and Kilian Q Weinberger. Densely connected convolutional networks. In *Proceedings of the IEEE conference on computer vision and pattern recognition*, pages 4700–4708, 2017.
- [Johnson *et al.*, 2018] Justin Johnson, Agrim Gupta, and Li Fei-Fei. Image generation from scene graphs. In *Proceedings of the IEEE conference on computer vision and pattern recognition*, pages 1219–1228, 2018.
- [Kawahara *et al.*, 2018] Jeremy Kawahara, Sara Daneshvar, Giuseppe Argenziano, and Ghassan Hamarneh. Seven-point checklist and skin lesion classification using multi-task multimodal neural nets. *IEEE journal of biomedical and health informatics*, 23(2):538–546, 2018.
- [Kim *et al.*, 2018] Been Kim, Martin Wattenberg, Justin Gilmer, Carrie Cai, James Wexler, Fernanda Viegas, et al. Interpretability beyond feature attribution: Quantitative testing with concept activation vectors (tcav). In *International conference on machine learning*, pages 2668–2677. PMLR, 2018.
- [Kindermans *et al.*, 2019] Pieter-Jan Kindermans, Sara Hooker, Julius Adebayo, Maximilian Alber, Kristof T. Schütt, Sven Dähne, Dumitru Erhan, and Been Kim. *The (Un)reliability of Saliency Methods*, pages 267–280. Springer International Publishing, Cham, 2019.
- [Koh *et al.*, 2020] Pang Wei Koh, Thao Nguyen, Yew Siang Tang, Stephen Mussmann, Emma Pierson, Been Kim, and Percy Liang. Concept bottleneck models. In *International conference on machine learning*, pages 5338–5348. PMLR, 2020.
- [Lee and Seung, 1999] Daniel D Lee and H Sebastian Seung. Learning the parts of objects by non-negative matrix factorization. *nature*, 401(6755):788–791, 1999.
- [Luo *et al.*, 2020] Dongsheng Luo, Wei Cheng, Dongkuan Xu, Wenchao Yu, Bo Zong, Haifeng Chen, and Xiang Zhang. Parameterized explainer for graph neural network. *Advances in neural information processing systems*, 33:19620–19631, 2020.

- [Mendonça *et al.*, 2013] Teresa Mendonça, Pedro M Ferreira, Jorge S Marques, André RS Marcal, and Jorge Rozeira. Ph 2-a dermoscopic image database for research and benchmarking. In *2013 35th annual international conference of the IEEE engineering in medicine and biology society (EMBC)*, pages 5437–5440. IEEE, 2013.
- [Oikarinen *et al.*, 2023] Tuomas Oikarinen, Subhro Das, Lam M Nguyen, and Tsui-Wei Weng. Label-free concept bottleneck models. *arXiv preprint arXiv:2304.06129*, 2023.
- [Patrício *et al.*, 2023] Cristiano Patrício, João C Neves, and Luis F Teixeira. Coherent concept-based explanations in medical image and its application to skin lesion diagnosis. In *Proceedings of the IEEE/CVF conference on computer vision and pattern recognition*, pages 3799–3808, 2023.
- [Petsiuk *et al.*, 2018] Vitali Petsiuk, Abir Das, and Kate Saenko. Rise: Randomized input sampling for explanation of black-box models. *arXiv preprint arXiv:1806.07421*, 2018.
- [Samek *et al.*, 2016] Wojciech Samek, Alexander Binder, Grégoire Montavon, Sebastian Lapuschkin, and Klaus-Robert Müller. Evaluating the visualization of what a deep neural network has learned. *IEEE transactions on neural networks and learning systems*, 28(11):2660–2673, 2016.
- [Sandler *et al.*, 2018] Mark Sandler, Andrew Howard, Menglong Zhu, Andrey Zhmoginov, and Liang-Chieh Chen. Mobilenetv2: Inverted residuals and linear bottlenecks. In *Proceedings of the IEEE conference on computer vision and pattern recognition*, pages 4510–4520, 2018.
- [Sarkar *et al.*, 2022] Anirban Sarkar, Deepak Vijaykeerthy, Anindya Sarkar, and Vineeth N Balasubramanian. A framework for learning ante-hoc explainable models via concepts. In *Proceedings of the IEEE/CVF conference on computer vision and pattern recognition*, pages 10286–10295, 2022.
- [Selvaraju *et al.*, 2017] Ramprasaath R Selvaraju, Michael Cogswell, Abhishek Das, Ramakrishna Vedantam, Devi Parikh, and Dhruv Batra. Grad-cam: Visual explanations from deep networks via gradient-based localization. In *Proceedings of the IEEE international conference on computer vision*, pages 618–626, 2017.
- [Smilkov *et al.*, 2017] Daniel Smilkov, Nikhil Thorat, Been Kim, Fernanda Viégas, and Martin Wattenberg. Smoothgrad: removing noise by adding noise. *arXiv preprint arXiv:1706.03825*, 2017.
- [Sundararajan *et al.*, 2017] Mukund Sundararajan, Ankur Taly, and Qiqi Yan. Axiomatic attribution for deep networks. In *International conference on machine learning*, pages 3319–3328. PMLR, 2017.
- [Tschandl *et al.*, 2018] Philipp Tschandl, Cliff Rosendahl, and Harald Kittler. The ham10000 dataset, a large collection of multi-source dermoscopic images of common pigmented skin lesions. *Scientific data*, 5(1):180161, 2018.
- [Veličković *et al.*, 2017] Petar Veličković, Guillem Cucurull, Arantxa Casanova, Adriana Romero, Pietro Lio, and Yoshua Bengio. Graph attention networks. *arXiv preprint arXiv:1710.10903*, 2017.
- [Ying *et al.*, 2019] Zhitao Ying, Dylan Bourgeois, Jiaxuan You, Marinka Zitnik, and Jure Leskovec. Gnnexplainer: Generating explanations for graph neural networks. *Advances in neural information processing systems*, 32, 2019.
- [Yuksekgonul *et al.*, 2022] Mert Yuksekgonul, Maggie Wang, and James Zou. Post-hoc concept bottleneck models. *arXiv preprint arXiv:2205.15480*, 2022.